small methods
www.small-methods.com

Magnetically Selective Versatile Transport of Microrobotic Carriers

Xinghao Hu, Keonmok Kim, Abbas Ali, Hyeonseol Kim, Yumin Kang, Jonghwan Yoon, Sri Ramulu Torati, Venu Reddy, Mi-Young Im, Byeonghwa Lim, and CheolGi Kim**

Field-driven transport systems offer great promise for use as biofunctionalized carriers in microrobotics, biomedicine, and cell delivery applications. Despite the construction of artificial microtubules using several micromagnets, which provide a promising transport pathway for the synchronous delivery of microrobotic carriers to the targeted location inside microvascular networks, the selective transport of different microrobotic carriers remains an unexplored challenge. This study demonstrated the selective manipulation and transport of microrobotics along a patterned micromagnet using applied magnetic fields. Owing to varied field strengths, the magnetic beads used as the microrobotic carriers with different sizes revealed varied locomotion, including all of them moving along the same direction, selective rotation, bidirectional locomotion, and all of them moving in a reversed direction. Furthermore, cells immobilized with magnetic beads and nanoparticles also revealed varied locomotion. It is expected that such steering strategies of microrobotic carriers can be used in microvascular channels for the targeted delivery of drugs or cells in an organized manner.

1. Introduction

Microrobotic carriers such as colloidal particles, liquid droplets or synthetic motors have promising functions in the fields of drug delivery, molecular or cells transport in biomedical applications, and lab-on-a-chip devices.[1–6] Magnetic field powered-transport of the microrobotic carriers offers intrinsic advantages such as high penetration and safety to biological entities. For example, a neutrophil-based microrobot can be magnetically actuated to realize drug delivery to malignant glioma in vivo.[7] Further, magnetic microrollers can be functionalized to transport drugs into cells and propelled against physiologically relevant blood flow.[8–13] In addition, the use of ferrofluid droplets as soft microrobotic carriers has demonstrated effective cargo delivery in confined regions for future biomedical applications.[14–17] However, achieving reliable transport of magnetic microrobotic carriers over long distances remains challenging owing to difficult navigation and complex fluid environments.

Tubular magnetic medical catheters have shown promise in delivering drugs to hard-to-access regions inside the human body.[18–20] However, the miniaturization to micrometer scale remains challenging. Inspired by Kinesins, which can walk along microtubules,[21,22] an artificial magnetic microtubule was constructed as a specific transport pathway for the directional delivery of microrobotic carriers.[23] The microrobotic carriers travel an order of magnitude faster than when using the traditional transport method under the same magnetic driving frequency; they can travel against strong fluid flows. However, the artificial microtubule utilizes discrete micromagnets as stepping stones to guide carriers, which restricts the transport of carriers that are smaller than the gap between the micromagnets, posing a limitation to their effective movement.

Thin-film-patterned micromagnets have consecutive structures that enable the simultaneous transport of microrobotic carriers. Here, the microrobottic carriers can be reasonably approximated as magnetic point dipoles. When they are exposed to magnetic fields with inhomogeneous distributions on the scale of the carrier size, the microrobotic carriers move towards the nearest locations of the minima of the magnetostatic potential energy, which are induced by the patterned micromagnets. Based on the

X. Hu, K. Kim, A. Ali, H. Kim, Y. Kang, J. Yoon, S. R. Torati, V. Reddy, M.-Y. Im, C. Kim
Department of Physics and Chemistry
DGIST
Daegu 42988, Republic of Korea
E-mail: cgkim@dgist.ac.kr
X. Hu
State Key Laboratory of Solidification Processing
Center of Advanced Lubrication and Seal Materials
Northwestern Polytechnical University
Xi'an 710072, China
M.-Y. Im
Center for X-ray Optics
Lawrence Berkeley National Laboratory Berkeley
Berkeley, CA 94720, USA
B. Lim
Department of Smart Sensor Engineering
Andong National University
Andong 36729, Republic of Korea
E-mail: limbh@anu.ac.kr

The ORCID identification number(s) for the author(s) of this article can be found under https://doi.org/10.1002/smtd.202301495

DOI: 10.1002/smtd.202301495

geometry designs of micromagnet ladders or negative patterns and in combination with three-dimensional structures as well, the microrobotic carriers can be controlled simultaneously in a specific direction.[24–27] Furthermore, the introduction of circuit concepts allows for programmable active transport of the microrobotic carriers under a magnetic in-plane field with a combination of current lines or a pulsed out-of-plane field, which can produce instantaneous potential energy for the microrobotic carriers to cross the energy barrier over the micromagnet. A nonmagnetic gap could also cause an energy barrier to hinder particle transportation. However, the nonlinear dynamics of microrobotic carriers moving around a micromagnet have revealed three different dynamical modes: phase-locked mode at low driving frequencies, phase-slipping mode above the first critical frequency, and phase-insulated mode above the second critical frequency. In the phase-slipping mode, the microrobotic carrier is able to jump, thus crossing the energy barrier over the nonmagnetic gap.[28,29] Based on the different dynamic motions of the microrobotic carriers with varied sizes, they could be separated by the nonmagnetic gap into different micromagnet tracks. Although the passive separation of the microrobotic carriers could be executed by the carrier dynamics, selective transport of the microrobotic carriers along a specific pathway to deliver multiple cells or drugs in an orderly manner remains under exploration.

This study demonstrated that microrobotic carriers with different sizes could be selectively manipulated and transported along the micromagnet pathway by tuning the magnetic field strength. Under sufficiently high field strength, the magnetic beads (2.8 and 5.8 μm in diameter) as microrobotic carriers all moved along the positive direction of the micromagnet pathway. With the decrease in the field strength, the two types of beads exhibited transitional locomotion from traversal in the positive direction to rotation, bidirectional locomotion, and traversal along the negative direction. Furthermore, cells immobilized with magnetic beads and nanoparticles also exhibited such versatile transport. Based on the nonsynchronous locomotion, two types of cells enabled selective transport along the specific pathway via the regulation of the applied magnetic field. Thus, the proposed transport strategy of the microrobotic carriers could realize the directional delivery of drugs or cells using micromagnet constructed artificial microtubule.

2. Results and Discussion

2.1. Mechanism of Selective Versatile Transport by Micromagnet Pathway

The autonomous separation of magnetic beads or cells to different tracks has been demonstrated using a navigating gate, which creates an artificial potential energy barrier at the gap between the discrete micromagnets. Furthermore, the size and the magnetic susceptibility of the magnetic beads determine the separation efficiency.[28] Herein, the magnetic beads can be separated from each other in the prescribed path and only be successively transported to one outlet. The linear pathway comprised connected half-ellipse micromagnets with a bar-type structure, which could induce the directional movement of the beads under a rotating in-plane field. However, in the case of a linear pathway comprising full-disk micromagnets, the beads moved in both directions.

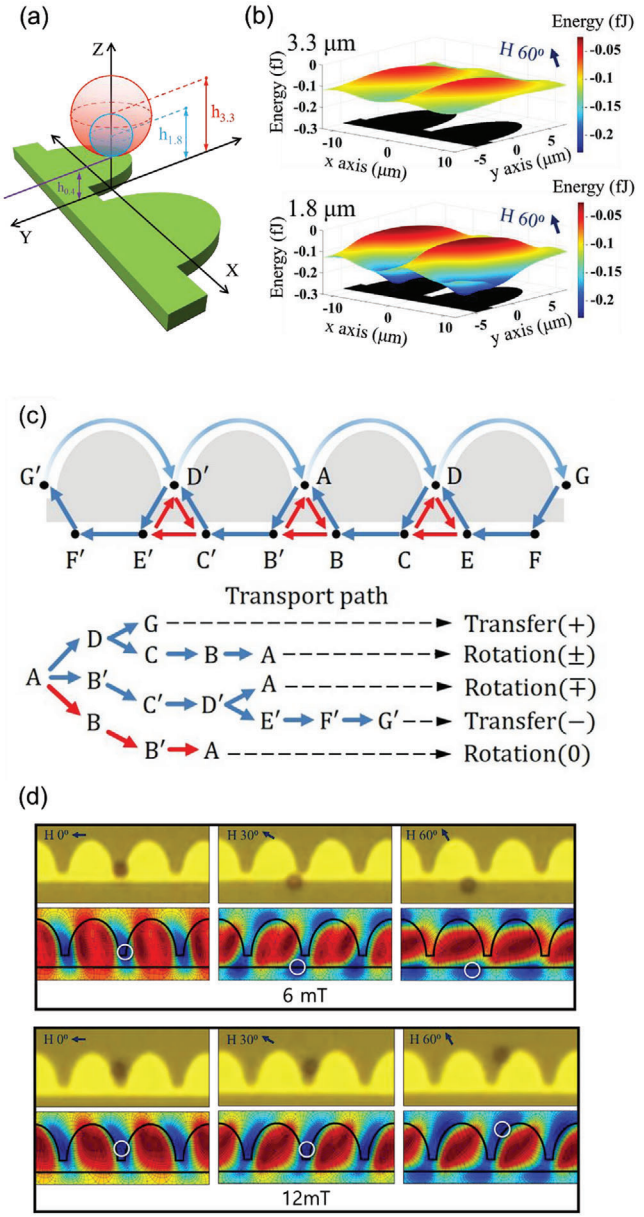

Figure 1. Schematic of magnetic bead transport along micromagnet pathway. a) Schematic representation of the vertical height calculation for the magnetic bead of different sizes. The vertical height of $h_{2.8}$ (bead with 2.8 μm diameter) and $h_{5.8}$ (bead with 5.8 μm diameter) is the sum of the bead radius and the thickness of the passivation layer. b) Magnetostatic potential energy distribution at different heights. The blue color represents the deeper potential well. The applied field strength is 6 mT, and the field direction is 60° to the X-axis. c) Schematic varied transport paths of the beads. d) Potential energy distribution and the experimental images indicating that the bead moves along reverse paths under different field strengths (6 and 12 mT). The field direction is 60° to the X-axis.

Fundamentally, the magnetic beads moved along the gradient of the magnetic fields or potential energy to the maximum or the minimum. Considering the 3D distribution of "stray fields" produced by micromagnets, the bead was oriented from its center point to the micromagnet surface according to the vertical height.

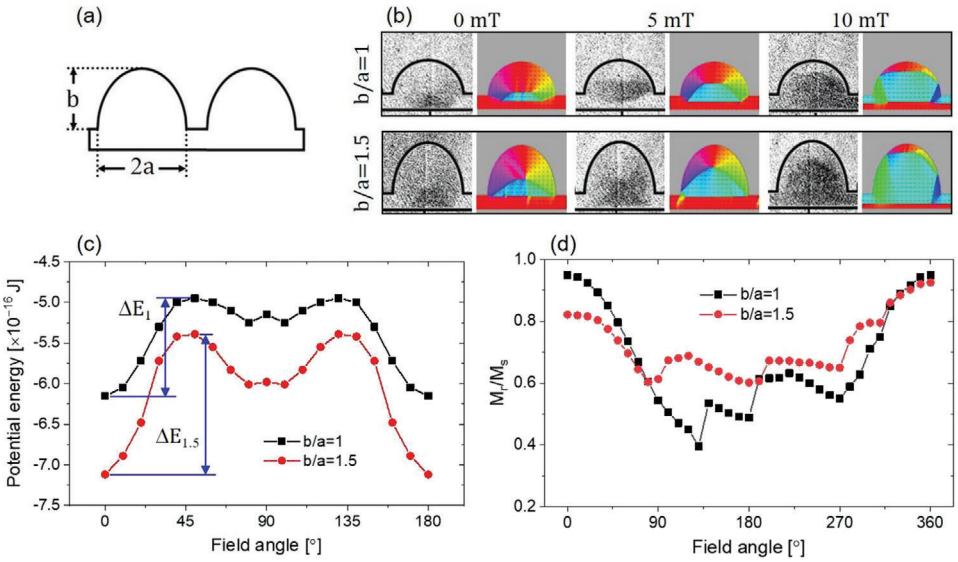

Figure 2. Magnetization variations of the micromagnets. a) The schematic explanation of the aspect ratio of the half-ellipse determines the micromagnet shape. b) Observed and simulated magnetic domain structures depending on the aspect ratio of the half-ellipse micromagnet and the applied field strength. The applied field direction is along the X-axis. c) Potential energy minima around the half-ellipse edge of the micromagnet at varied field angles calculated through simulation. The applied field strength is 10 mT. The potential energy deviation (ΔE) to the micromagnet with the aspect ratio b/a = 1.5 is larger than the micromagnet with the aspect ratio b/a = 1. This indicates the presence of a larger energy barrier to transport magnetic beads around the micromagnet (b/a = 1.5). d) Variation of magnetization ratio between the field directional component (M_r) and the saturated magnetization (M_s) varies with the applied field angle and the micromagnet aspect ratio. The applied field strength is 10 mT. The simulation result shows that the micromagnet (b/a = 1.5) has a smaller magnetization ratio than that of the aspect ratio (b/a = 1) at low angles (< 90°), which respects the magnetic shape anisotropy. This indicates that the forward movement of the magnetic beads around the half-ellipse edge of the micromagnet (b/a = 1) is easier compared with that of the micromagnet (b/a = 1.5).

The vertical height is the sum of the bead radius and the thickness of the passivation layer on the micromagnets (**Figure** 1a). The depth and gradient of the potential energy well in a landscape distribution depend on the vertical height and the applied field strength. Figure 1b shows the different potential energy landscape at 1.8 and 3.3 μm height for applied field strength of 6 mT and field direction of 60° to the X-axis. As evident, the multi-sized beads experienced different potential energies.

Figure 1c illustrates the five types of transport paths for beads moving along the micromagnet pathway. These path variations are influenced by the magnetic domains of the micromagnets and the distribution of potential energy. When the applied field strength was sufficiently high, the micromagnets become adequately magnetized, causing the magnetic beads to move along the positive direction (Transfer (+)) along the curved micromagnet pathway, in case of an in-plane field rotating in the clockwise direction. However, if the magnetic field strength decreases below a critical threshold, the micromagnet might not be sufficiently magnetized. In such cases, although bead transport along the A-D path is possible, continuous movement between micromagnets does not occur. Consequently, the beads rotate around a single micromagnet, either at the front or back of their current position (Rotation (±), (∓)). Furthermore, reducing the magnetic field intensity while maintaining the same rotation direction leads to a shift in the potential energy change of the micromagnets from the A-D to the A-B' path. Consequently, this change leads to the transportation of the magnetic beads in the negative direction (Transfer (-)). Lastly, with a further reduction in magnetic field intensity, the potential energy change of the micromagnets shifts from the B'-C' path to the B'-B path. As a result, rotation is confined to the area between two micromagnets (Rotation (0)). Figure 1d experimentally and theoretically demonstrated the potential energy distribution at 0°, 30°, and 60° along the X-axis under 6 and 12 mT magnetic fields. It shows that as the magnetic field rotates from 30° to 60°, the magnetic beads follow either an A-D or A-B' path, depending on the field's intensity.

To achieve the varied transport paths to the magnetic beads mentioned above, it is impossible to use the micromagnet pathway comprising the half disks with the traditional shape (b/a = 1 as the aspect ratio, **Figure** 2a). Thus, the geometric structure of the essential element of a single micromagnet is modified to obtain suitable stray fields or potential energy distribution from the micromagnet. Figure 2b presents the observed and simulated magnetic domain structures of the micromagnet with aspect ratios of b/a = 1 and 1.5 under the applied fields of 0, 5, and 10 mT in the direction along the X-axis. We initially observed the magnetic domain dynamics to simulate potential energy changes through magnetic domain alterations. The simulation parameters were adjusted accordingly since these observations were feasible only in the X-axis direction. This approach showed that observation and simulation have a good match. As shown in Figure 2c, the potential energy minima based on the domain simulation were obtained depending on the applied field angles, and the field strength was 10 mT. It indicated that the potential energy deviation (ΔE) of the micromagnet with an aspect ratio of b/a = 1.5 was larger than that of the micromagnet with an aspect ratio of b/a = 1. Consequently, a larger energy barrier was observed when transporting magnetic beads

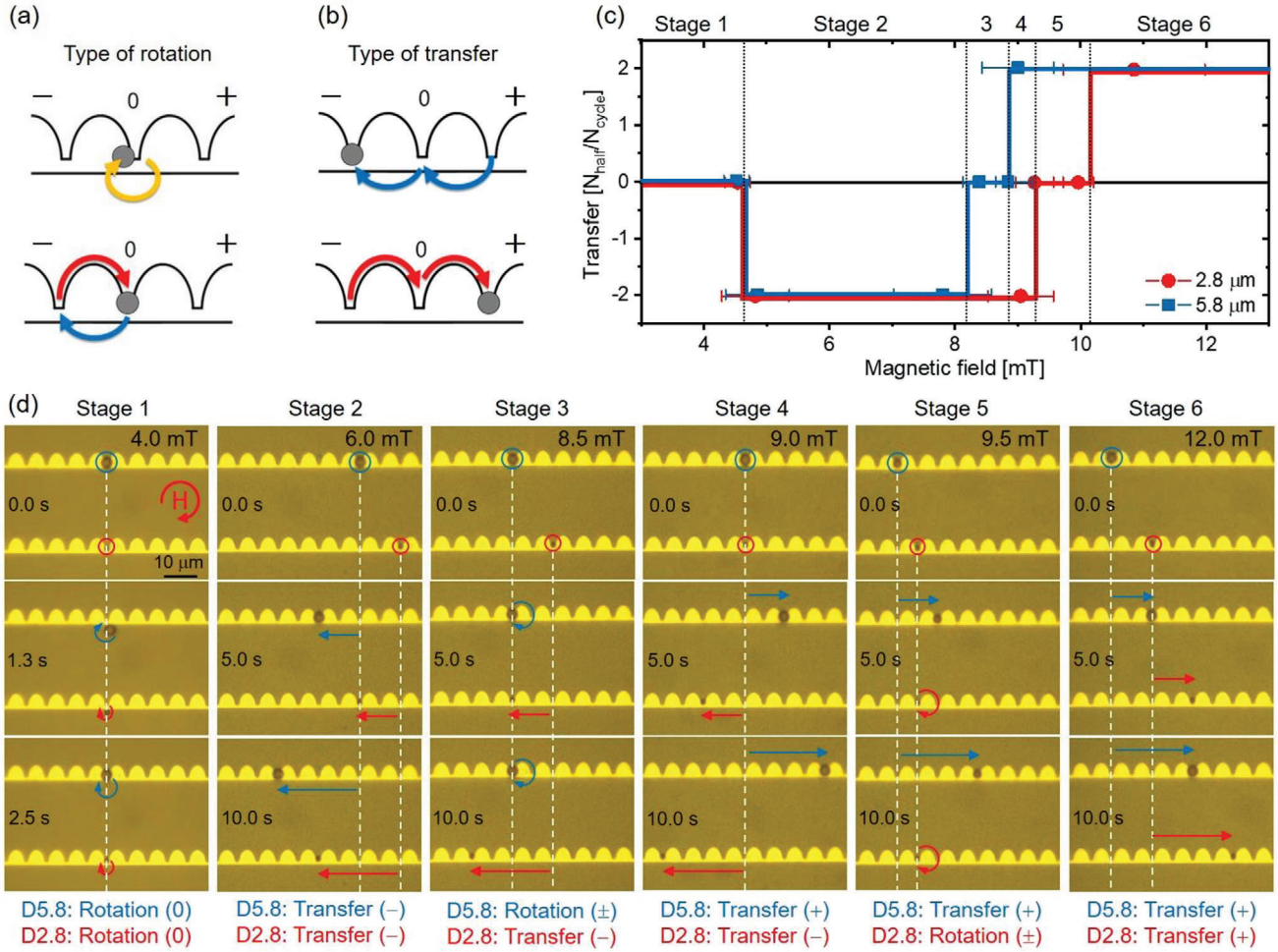

Figure 3. Selective transport of magnetic beads through variations of the field strength. The bead locomotion is classified as a) Rotation and b) Transfer. Furthermore, each locomotion can be classified into two forms. c) Transport paths of the beads depending on the field strength. The switching field range is divided into six stages for the beads with diameters of 2.8 and 5.8 μm. d) Variation of bead locomotion in the order of rotation (0) → Transfer (−) → Rotation (±)/(∓) → Transfer (+) with an increase in the field strength increases. The rotating field frequency is 0.2 Hz.

around the micromagnet (b/a = 1.5), which is consistent with the magnetization ratio between the field directional component (M_r) and the saturated magnetization (M_s). As shown in Figure 2d, the micromagnet with the aspect ratio b/a = 1.5 had a smaller magnetization ratio compared with that having b/a = 1 at low angles (< 90°), which represent the magnetic shape anisotropy. This indicated that the forward movement of the magnetic beads around the half-ellipse edge of the micromagnet (b/a = 1) was easier compared to that with the micromagnet (b/a = 1.5).

2.2. Selective Transport of Multi-Sized Magnetic Beads

The magnetic beads reveal four types of locomotion moving along the micromagnet pathway with an aspect ratio of b/a = 1.5 under the rotating field in a clockwise direction, as shown in **Figure** 3a (Rotation (0) and Rotation (±)/(∓)) and Figure 3b (Transfer (+) and Transfer (−)). The four types of locomotion of the magnetic beads can be switched by the applied field strength. For example, when the applied field increased from 4 mT (Figure 3c), the bead locomotion (2.8 μm diameter) started from the type of rotation (0), successively shifting to Transfer (−) under the applied field of 6 mT (Figure S1, Supporting Information), Rotation (±)/(∓) under the applied field of 10 mT (Figure S2, Supporting Information), and Transfer (+) types under the applied field of 12 mT (Figure S3, Supporting Information). Considering two kinds of magnetic beads with diameters of 2.8 and 5.8 μm, the switching field range for the combination of locomotion types was divided into six stages as shown below.

Stage 1 (≈4.0 mT): both beads are were in the Rotation (0) type of locomotion, moving at with the gap between two micromagnets (Movie S1, Supporting Information).

Stage 2 (≈6.0 mT): both of beads are were transported in the negative direction of the micromagnet pathway (Movie S2, Supporting Information), Transfer (−).

Stage 3 (≈8.5 mT): the beads with 5.8 μm diameter exhibited the locomotion of the rotation (±)/(∓) type, but however, the beads with 2.8 μm diameter exhibited the locomotion of the Transfer (−) type (Movie S3, Supporting Information).

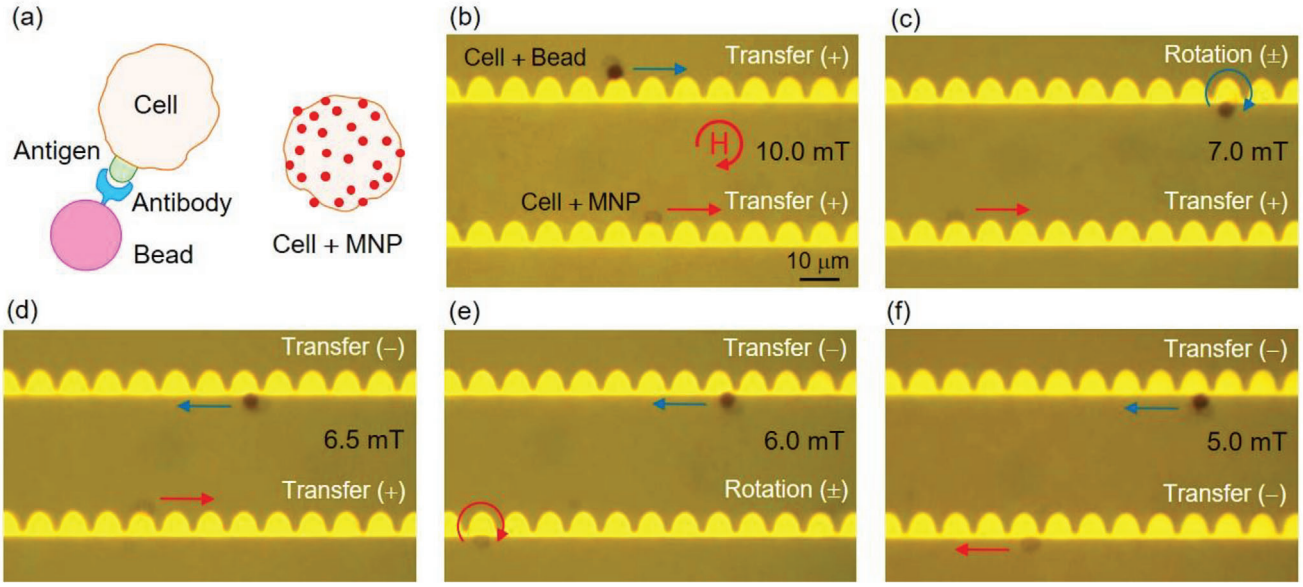

Figure 4. Selective transport of cells. a) Schematic for T Lymphocytes conjugated to magnetic beads, and B Lymphocytes conjugated to magnetic nanoparticles (MNP). b) Cell-bead complex and the cell-MNP complex are both in the transfer (+) stage under the 10.0 mT field. c) Cell-bead complex and the cell-MNP complex in rotation (±) and transfer (+) stage under 7.0 mT field, respectively. d) Cell-bead complex in transfer (−) stage and cell-MNP complex is in transfer (+) stage under 6.5 mT field. e) Cell-bead complex in transfer (−) stage and cell-MNP complex in rotation (±) stage under 6.0 mT field. f) Cell-bead and cell-MNP complex both in transfer (−) stage under 5.0 mT field.

Stage 4 (≈9.0 mT): the beads with 5.8 μm diameter were transported along the positive direction of the micromagnet pathway (Transfer (+))., but the beads with 2.8 μm diameter still exhibited the locomotion of the Transfer (−−) type. It shows that the two kinds of beads had bidirectional locomotion (Movie S4, Supporting Information).

Stage 5 (≈9.5 mT): the beads with 5.8 μm diameter exhibited the locomotion of the Transfer (+) type; however, but the beads with 2.8 μm diameter shifted to the locomotion of Rotation (±)/(∓) type (Movie S5, Supporting Information).

Stage 6 (≈12.0 mT): both beads are exhibited by the Transfer (+) type of locomotion, moving in along the positive direction of the micromagnet pathway (Movie S6, Supporting Information). Figure 3d presents the experimental images of the bead locomotion at each stage, when the applied field strengths were 4.0, 6.0, 8.5, 9.0, 9.5, and 12.0 mT, respectively. The applied field frequency was 0.2 Hz. Here, two micromagnet pathways were utilized to demonstrate the varied locomotion in six stages, in order to eliminate the influences of the two types of beads from each other. A single micromagnet pathway made it possible to realize the selective versatile transport of the magnetic beads.

2.3. Selective Transport of Cells

Lymphocytes are a type of white blood cell, which help facilitate the immune system of human beings to fight cancer or foreign bacteria. Therefore, we used T and B Llymphocytes to demonstrate the selective versatile transport of cells moving along the micromagnet pathway. This could be helpful to aid in the development of the cell therapy system for the hard-to-access regions inside the human body. Based on the interaction between an antigen and antibody (**Figure** 4a), magnetic beads and nanoparticles were immobilized on the T and B Llymphocytes, respectively. Due to the different sizes and magnetic properties of the immobilized cells conjugated with the magnetic beads and nanoparticles, two kinds types of cells can be manipulated in varied locomotion as well as in addition to the two kinds types of beads above.

Figure 4b presents indicate that both complexes of cell+bead and cell+nanoparticles have exhibited transfer in the positive direction along the micromagnet pathway, under the applied rotating field of 10.0 mT in the clockwise direction (Movie S7, Supporting Information). The rotating frequency was 0.2 Hz. When the field strength reduces to 7.0 mT, the complex of cell+bead shifts to the locomotion of Rotation (±) type (Movie S8, Supporting Information). In addition, when the field strength reaches 6.5, 6.0, and 5.0 mT, the complex of cell+bead inhibits the locomotion of the Transfer (−) type constantly (Movie S9, Supporting Information). However, but the complex of cell+nanoparticles shifted from the Transfer (+) type to the Rotation (±) type (Movie S10, Supporting Information), and the Transfer (−) type (Movie S11, Supporting Information), respectively. It shows that Thus, owing to different magnetic immobilizations, the cells could be transported in a controllable manner along a micromagnet pathway.

3. Conclusion

This study demonstrated a selective versatile transport strategy of magnetic microrobotic carriers, moving along a half-ellipse micromagnet pathway under the control of applied field strength. The multi-sized magnetic beads (2.8 and 5.8 μm in diameter) were separated and manipulated in varied locomotion (isotropic, bidirectional, and march on the spot). As the microrobotic

carriers, the magnetic beads or nanoparticles could implement directional and precise delivery of cells or drugs along a specific track. In addition, to combine with existing microfabrication technologies, the micromagnet pathway could be utilized with a microcatheter to reach narrow microvascular channels for robust and precise drug delivery with organized manipulation, which enables to overcome the intrinsic limitations of tubular catheters and freely swimming microrobots.[29,30]

4. Experimental Section

Fabrication of Micromagnets and Applied Magnetic Fields: Patterned micromagnets were fabricated on silicon wafers using conventional photolithography and a sputtering system. A photoresist (AZ 5214 E) and UV mask aligner (MIDAS, MDA-400S) were used to produce the patterns. First, 100 nm thick Ni83Fe17 (Kojundo Chemical Laboratory Co., Ltd., Japan) was deposited via DC magnetron sputtering. Next, thereafter, the samples were coated with 500 nm thick Teflon (DuPont, Grade 601S2-100-6) via spin-coating (3500 rpm for 30 s), to protect the micromagnets in the fluid environment and diminish surface adhesion forces.

The rotating in-plane magnetic field was produced by using four ferrite core solenoids, which were arranged at mutually orthogonal axes in the x–y plane of the substrate. Two current sources were controlled by using the LabVIEW program to supply sinusoidal waveforms to each solenoid coil along the orthogonal axes, whose phase difference was adjusted by 90° to generate a rotating magnetic field.

Magnetic Domain Measurement and Simulation: To interpret a micromagnet that moves beads based on the strength of the magnetic field, the magnetic domain of the patterned micromagnets was measured and compared to simulations. Magnetic transmission soft X-ray microscopy (MTXM) was used to perform domain measurements. Because of the beam size limitation of the MTXM, the micromagnet size was reduced to half of that of the actual structure while maintaining the aspect ratio. The simulation was conducted using the MuMax3 software (where an exchange stiffness $A_{ex} = 13\times10^{-12}$ Jm^{-1}, saturation magnetization $M_s = 860$ kAm^{-1}, damping constant a = 0.1, zero magnetocrystalline anisotropy, and cell dimensions of 20×20×20 nm^3 were used as standard material parameters). The magnetostatic potential energy on a superparamagnetic particle was obtained using: $U(\vec{r}, t) = -\chi_V V\vec{B}^2/2\mu_0$; where χ_V is the volumetric magnetic susceptibility of superparamagnetic particles; V is the volume of the particle; $\vec{B}$ is the total magnetic field at the particle center, and μ_0 is the vacuum permeability.

Magnetic Particles and Immobilization of Cells: T and B lymphocytes were obtained from the spleens of C57BL6 mice (KOATECH, Pyeongtaek, Korea). Magnetic beads with diameters of 4.5 µm (Dynabeads mouse Pan T, Thy1.2) were purchased from Invitrogen. Magnetic nanoparticles with 50 nm diameter conjugated with CD45R (B220, B lymphocytes) were purchased from Miltenyi Biotec. Based on the interaction between antigens on the lymphocytes and corresponding antibodies on the magnetic beads and nanoparticles, the magnetic immobilization of cells was executed. In addition, the superparamagnetic beads of 2.8 µm diameter (Dynabeads M-280 Streptavidin) and 5.8 µm diameter (CM01N/11 374) were purchased from the Invitrogen and Bangs Laboratories, respectively.

Supporting Information

Supporting Information is available from the Wiley Online Library or from the author.

Acknowledgements

X.U., K.K., and A.A. equally contributed to the paper. This research was supported by the National Research Foundation of Korea (NRF) grant funded by the Korean government (MSIT) (2018R1A5A1025511). X.H. would like to thank the Shaanxi Science and Technology Program for financial support (QCYRCXM-2022-235 and 2023-JC-YB-576).

Conflict of Interest

The authors declare no conflict of interest.

Data Availability Statement

The data that support the findings of this study are available on request from the corresponding author. The data are not publicly available due to privacy or ethical restrictions.

Keywords

applied magnetic field, artificial microtubule, micromagnet, microrobotic carrier, single-cell delivery

Received: November 5, 2023
Revised: December 28, 2023
Published online: February 2, 2024

[1] B. Wang, K. Kostarelos, B. J. Nelson, L. Zhang, *Adv. Mater.* **2021**, *33*, 2002047.
[2] J. Li, B. Esteban-Fernández de Ávila, W. Gao, L. Zhang, J. Wang, *Sci. Rob.* **2017**, *2*, eaam6431.
[3] B. Yigit, Y. Alapan, M. Sitti, *Adv. Sci.* **2019**, *6*, 1801837.
[4] B. J. Nelson, I. K. Kaliakatsos, J. J. Abbott, *Annu. Rev. Biomed. Eng.* **2010**, *12*, 55.
[5] D. Ahmed, T. Baasch, N. Blondel, N. Läubli, J. Dual, B. J. Nelson, *Nat. Commun.* **2017**, *8*, 770.
[6] B. Zhang, *Nat. Rev. Mater.* **2018**, *3*, 257.
[7] H. Zhang, Z. Li, C. Gao, X. Fan, Y. Pang, T. Li, Z. Wu, H. Xie, Q. He, *Sci. Rob.* **2021**, *6*, eaaz9519.
[8] F. Mou, Q. Xie, J. Liu, S. Che, L. Bahmane, M. You, J. Guan, *Natl Sci Rev* **2021**, *8*, nwab066.
[9] L. Wang, X. Hao, Z. Gao, Z. Yang, Y. Long, M. Luo, J. Guan, *Interdiscip. Mater.* **2022**, *1*, 256.
[10] Y. Alapan, U. Bozuyuk, P. Erkoc, A. C. Karacakol, M. Sitti, *Sci. Rob.* **2020**, *5*, eaba5726.
[11] U. Bozuyuk, A. Aghakhani, Y. Alapan, M. Yunusa, P. Wrede, M. Sitti, *Nat. Commun.* **2022**, *13*, 6289.
[12] T. Li, S. Yu, B. Sun, Y. Li, X. Wang, Y. Pan, C. Song, Y. Ren, Z. Zhang, K. T. Grattan, *Sci. Adv.* **2023**, *9*, eadg4501.
[13] P. Wrede, O. Degtyaruk, S. K. Kalva, X. L. Deán-Ben, U. Bozuyuk, A. Aghakhani, B. Akolpoglu, M. Sitti, D. Razansky, *Sci. Adv.* **2022**, *8*, eabm9132.
[14] H. Xie, M. Sun, X. Fan, Z. Lin, W. Chen, L. Wang, L. Dong, Q. He, *Sci. Rob.* **2019**, *4*, eaav8006.
[15] J. Yu, D. Jin, K.-F. Chan, Q. Wang, K. Yuan, L. Zhang, *Nat. Commun.* **2019**, *10*, 5631.
[16] X. Fan, X. Dong, A. C. Karacakol, H. Xie, M. Sitti, *Proc. Natl. Acad. Sci. USA* **2020**, *117*, 27916.
[17] X. Fan, Y. Jiang, M. Li, Y. Zhang, C. Tian, L. Mao, H. Xie, L. Sun, Z. Yang, M. Sitti, *Sci. Adv.* **2022**, *8*, eabq1677.
[18] B. Wang, K. F. Chan, K. Yuan, Q. Wang, X. Xia, L. Yang, H. Ko, Y.-X. Wang, J. J. Y. Sung, P. W. Y. Chiu, *Sci. Rob.* **2021**, *6*, eabd2813.

[19] Y. Kim, G. A. Parada, S. Liu, X. Zhao, *Sci. Rob.* **2019**, *4*, eaax7329.
[20] J. Hwang, S. Jeon, B. Kim, J. Kim, C. Jin, A. Yeon, B. J. Yi, C. H. Yoon, H. J. Park, S. Pané, *Adv. Healthcare Mater.* **2022**, *11*, 2102529.
[21] M. Schliwa, G. Woehlke, *Nature* **2003**, *422*, 759.
[22] N. Hirokawa, Y. Noda, Y. Tanaka, S. Niwa, *Nat. Rev. Mol. Cell Biol.* **2009**, *10*, 682.
[23] H. Gu, E. Hanedan, Q. Boehler, T.-Y. Huang, A. J. Mathijssen, B. J. Nelson, *Nature Machine Intelligence* **2022**, *4*, 678.
[24] A. Ali, H. Kim, S. R. Torati, Y. Kang, V. Reddy, K. Kim, J. Yoon, B. Lim, C. Kim, *Small* **2023**, 2305528.
[25] S. R. Goudu, H. Kim, X. Hu, B. Lim, K. Kim, S. R. Torati, H. Ceylan, D. Sheehan, M. Sitti, C. Kim, *Nat. Commun.* **2021**, *12*, 3024.
[26] H. Kim, Y. Kang, B. Lim, K. Kim, J. Yoon, A. Ali, S. R. Torati, C. Kim, *Mater. Horiz.* **2022**, *9*, 2353.
[27] H. Kim, J. Yoon, A. Ali, S. R. Torati, Y. Kang, K. Kim, B. Lim, C. Kim, *J. Sci.: Adv. Mater. Devices* **2022**, *7*, 100482.
[28] X. Hu, S. R. Torati, H. Kim, J. Yoon, B. Lim, K. Kim, M. Sitti, C. Kim, *Small* **2019**, *15*, 1901105.
[29] J. Yoon, Y. Kang, H. Kim, S. R. Torati, K. Kim, B. Lim, C. Kim, *Adv. Sci.* **2022**, *9*, 2103579.
[30] H. Kim, B. Lim, J. Yoon, K. Kim, S. R. Torati, C. Kim, *Adv. Sci.* **2021**, *8*, 2100532.

